Near-Real-Time analysis of the ionospheric response to the 15 January 2022 Hunga Tonga-Hunga Ha'apai volcanic eruption

B. Maletckii[1] and E. Astafyeva[1]

[1] Université Paris Cité, Institut de Physique du Globe de Paris (IPGP), CNRS UMR 7154, 35-39 Rue Hélène Brion, 75013 Paris

Corresponding author: Boris Maletckii (maletckii@ipgp.fr)

Key Points:

- We suggest novel methods that detect and determine spatio-temporal characteristics of ionospheric disturbances in Near-Real-Time (NRT).
- We analyze large- and small-amplitude ionosphere response to the Tonga eruption in near (<2000 km) and far-field (~10000 km) in NRT scenario
- The amplitude of the dTEC/dt response to the Tonga eruption is comparable to the 2011 Tohoku earthquake and the 28 October 2003 solar flare

Abstract

We present a near-real-time (NRT) scenario of analysis of ionospheric response to the 15 January 2022 Hunga Tonga-Hunga Ha'apai eruption by using GNSS data in the near field (in the vicinity of the volcano), and in the far-field (Japan, North America and South America). We introduce a new method to determine instantaneous velocities using an interferometric approach and using the time derivative of the total electron content (TEC). Moreover, for the first time, we propose a novel method that automatically estimates the apparent propagation velocity of ionospheric disturbances from near-real-time travel-time diagrams. By using our new methods, we analyzed the dynamics of co-volcanic ionospheric disturbances generated by the Hunga-Tonga eruption, and we estimated the first propagation velocity in the near-field to be ~800-950 m/s, subsequently decreasing to ~600 m/s. Based on these values, we conclude that in the near-field, we detect ionospheric signatures of acoustic waves. In the far field, the apparent velocity of ionospheric disturbances was estimated to be between 277 and 365 m/s, which corresponds to the propagation of the Lamb wave. It is important to note that our new methods can successfully perform at low spatial resolution networks and with 30-sec cadence data. Also, they enable NRT spatio-temporal analysis of ionospheric TEC response to smaller-amplitude events.

1 Introduction

It is known that natural hazards, such as earthquakes, tsunamis, and volcanic eruptions generate acoustic and gravity waves that propagate upward in the atmosphere and ionosphere (e.g., Calais & Minster, 1995; Miyaki et al., 2002; Heki, 2006; Astafyeva, 2019). Ionospheric disturbances generated by volcanic eruptions are called co-volcanic ionospheric disturbances (co-VID). It is known that the co-VID are usually quasi-periodically shaped variations that occur ~10 to 45 min after the eruption onset, last for 1-1.5 hours, occur in the near field of a volcano (up to ~2000 km), and propagate at velocities in the range of 0.5 km/s - 1.1 km/s (Heki, 2006; Dautermann et al., 2009; Nakashima et al., 2016; Liu et al., 2017). Since the first-time detection of co-VID by Heki (2006), nowadays, the disturbances can be systematically detected by ground-based GNSS receivers. Shults et al. (2016) introduced for the first time a term "Ionospheric Volcanology" that refers to the use of ionospheric measurements for the interests of volcanology. For instance, from the co-VID measurements, it is possible to determine the location of an eruptive volcano, the time of eruption onset (Shults et al., 2016), and estimate volcanic eruption power (Heki, 2006; Dautermann et al., 2009; Manta et al., 2021). Ionosphere-based methods would complement conventional ones, which use data from nearby seismometers and infrasound stations. The accuracy of those conventional methods decreases in absence of instrumentation within ~100 km from a volcano. To make a new step toward ionospheric volcano monitoring and warning systems we must develop real or near-real-time (NRT) methods.

In this work, for the first time, we analyze spatio-temporal characteristics of ionospheric disturbances generated by the 15 January 2022 massive eruption of Hunga Tonga-Hunga Ha'apai

(HTHH) volcano in the NRT scenario. We suggest novel methods that automatically estimate the apparent propagation speed and direction of propagation of co-VID and other ionospheric disturbances, including small-amplitude ones, in near-real-time. This work is an important step toward automatised NRT detection of ionospheric disturbances.

2 Data and Methods

2.1 Total Electron Content by Global Navigation Satellite Systems

Global Navigation Satellite Systems (GNSS) are a helpful tool for ionospheric sounding. Its main advantage is good spatial and temporal resolution. Nowadays, 30-second data from over 9000 worldwide receivers are available on a daily basis. Each GNSS station can receive signals from 40+ GNSS satellites, providing numerous ionospheric observation points. High-rate data (1-second or less) are sparser (around 1000 receivers), however, local networks developed vastly in this direction over the last year. Phase measurements from dual-frequency GNSS receivers allow estimation of the ionospheric total electron content (TEC), which is equal to the number of electrons along a line-of-sight (LOS) between a satellite and a receiver:

$$TEC_{ij}\ (phase, slant)\ = \frac{1}{A} \times \frac{f_i^2 f_j^2}{f_i^2 - f_j^2} \times (L_i \lambda_i - L_j \lambda_j) \qquad (1)$$

where A = 40.308 m^3/s^2, L_i and L_j are phase measurements, λ_i and λ_j are wavelengths at the two the given frequencies (for Global Positioning System (GPS) i=1, j=2 and frequencies are 1575.42 and 1227.60 MHz, respectively). The TEC is measured in TEC units (TECu), 1 TECu = 10^{16} electrons/m^2.

We use the ionospheric thin shell approximation to calculate the spatial positions of ionospheric disturbances. The intersection points between the LOS and this shell (at a fixed altitude H_{ion}) are ionospheric pierced points (IPP). We use H_{ion} = 320 km since it is close to the maximum ionization height HmF2 (based on the nearest ionosonde station NIUE at 169.9E; 19.1S).

To study the co-VID signatures driven by the HHTH volcano eruption, we analyze data of 24 ground-based GNSS-receivers in the near-field, i.e., under ~2000 km away from the volcano. To extract the co-VID signatures from the TEC data series, researchers usually apply 1-4 mHz band-pass filters (Heki, 2006; Shults et al., 2016; Nakashima et al., 2016; Manta et al., 2021). However, in a real-time scenario it is not possible because of the following reasons: a) the impossibility to stack long series of data in NRT; b) such signal properties as arrival time, amplitude, and spectral components can be affected by the filter parameters (Maletckii et al., 2020). For NRT, we propose to use the TEC time derivative, which works as a high-pass filter and removes the bias and trend caused by the satellite orbit motion. In addition, our dTEC/dt approach will not modify the amplitude of the co-VID.

2.2. The "D1-GNSS-RT" method

By using the TEC time derivative approach, Maletckii and Astafyeva (2021a) introduced a method "D1-GNSS-RT" allowing to calculate spatio-temporal properties of traveling ionospheric disturbances (TID) in NRT (Figure 1). To detect TID, the "D1-GNSS-RT" method first analyses TEC data series to find the local maximum value (LMV). Then, it computes the cross-correlation function for each pair of time series around the LMV to calculate the difference in TID arrivals. Finally, based on these time shifts and by using an interferometric approach it estimates the horizontal velocities of TID propagation. The "D1-GNSS-RT" method was tested on several earthquakes but only showed good results with 1-sec data and on dense GNSS networks, such as Japan GEONET. The latter restrictions make it challenging to apply this method to the analysis of the co-VID generated by the HHTH volcanic eruption. The spatial coverage around the Tonga Islands is rather sparse, and only 16 out of 24 GNSS stations provide both 1-sec and 30-sec cadence data, while the others are limited to only 30-sec cadence data (Figure 2a). Besides, 30-sec dTEC/dt signals have smaller amplitudes and narrower spectral composition, which results in less pronounced signals as compared to 1-sec dTEC/dt data (Figure S1).

Here, for the first time, we introduce a new "D1-GNSS-RT" applicable to 30-sec data. The main developments are presented in Figure 1. They include: 1) increase of the LMV window to 7 minutes, 2) increase of the cross-correlation window to 24 minutes; 3) decrease of the threshold of the coefficient of the cross-correlation function down to 0.7. However, unfortunately, these new parameters modify the definition of NRT from 15 minutes for 1-sec data to 30 minutes for 30-sec data.

When the "D1-GNSS-RT" is not applicable (e.g., sparse GNSS coverage), the horizontal TID velocity can be estimated by using travel-time diagrams, or hodocrones, that present the TEC variations with respect to the source location and time. Similar to the D1-GNSS-RT, for NRT-TTD we also use the dTEC/dt parameter. As the source, we take the volcano position. From TTD, the velocity can be estimated as the slope, however, up to now, there was no NRT-compatible automatique method to do that. Here, for the first time, we developed a novel technique to fit the slope line in NRT.

2.3 The NRT TTD method and fitting technique

The automatic NRT TTD fitting technique consists of two stages: 1) the first maximum "picker" and 2) the "fitter" based on these maxima. To select the maximum along with all dTEC/dt values, we pick the values exceeding a standard deviation of the series and a threshold of 0.15 TECu. In the case of the multiple values in the 120-second windows, we chose the centered one in this window. We also remove outliers from the final list of maxima in the given series (values that can appear only with velocities exceeding 5 km/s).

We use the first maximum of each data series to fit the first velocity slope. They are sorted based on the source distance - from the closest to the farthest. By analyzing the velocity between

the current and previous maximum point we decide whether this maximum is "physically" suitable for the fitting process (velocity between two points should be in the range between 0.1 and 5 km/s and should not vary for more than 20% with respect to the velocity between two previous points; after picking the first 8 suitable maxima we add a new condition - the velocity should not change for more than 50% of the average velocity of all previous points). After the list of suitable points is finished, we fit the slope line by linear regression in these points.

In the case of the Quasi-NRT method, we added a second round for the picking process. After we obtain the first NRT velocity we compare all first maximum velocities with this value. If it lies in a 20% difference border interval, we pick this maximum. The new list of points is used for the Quasi-NRT fitting. Since the second round would require more time, we call this method "Quasi-NRT". However, the Quasi-NRT method seems to be more accurate, therefore it can be used to determine NRT-method accuracy in a particular case.

We implement these techniques to the HTHH eruption (Sections 3.1 and 3.2), but also to the M6.6 16 July 2007 Chuetsu earthquake, which is the smallest earthquake ever recorded in the ionosphere (Cahyadi and Heki, 2015) and the 4 August 2020 Beirut explosion (Section 3.3).

3 Results and Discussion

As shown recently, the explosive eruption of HTHH volcano produced quite a significant response in the ionosphere, and eruption-driven traveling ionospheric disturbances (TID) were observed as far as 20,000 km away from the volcano (Themens et al., 2022; Zhang et. al., 2022). The amplitude of the near-field response reached as high value as 5-8 TECu (Astafyeva et. al., 2022). In the case of the dTEC/dt parameter, we observe a peak-to-peak disturbance with the amplitude of ~8 TECu, which is extraordinary, as this value exceeds by a factor of 2.5-3 all previously recorded co-VID (Figure S2). Previously, disturbances with large dTEC/dt were only observed during the 2011 Tohoku-Oki earthquake and during the 28th October 2003 solar flare (Figure S2). The exceptionally high amplitude of the HTHH-driven co-VID can be explained by the fact that the eruption was accompanied by explosions of extreme power force (e.g., Matoza et al., 2022; Astafyeva et al., 2022). As known, the amplitude of NH-driven ionospheric disturbances depend on the magnitude of the initial forcing: larger earthquakes and volcanic eruptions generate larger disturbances in the ionosphere (Astafyeva et al., 2013; Cahyadi and Heki, 2015; Shults et al., 2016; Manta et al., 2022).

Below we use our newly developed methods and we estimate spatio-temporal evolution of HTHH-driven co-VID in the NRT scenario: the amplitude of the velocity, the azimuths of propagation, and the ionospheric source location.

3.1 Near-Field ionospheric disturbance due to the Tonga Eruption

3.1.1 Spatio-temporal characteristics of the co-VID from D1-GNSS-RT. Instantaneous velocities' field and source location.

Figure 2 (b-f) summarizes the results of the application of the D1-GNSS-RT method to the analysis of ionospheric TEC disturbances generated by the 15 January 2022 eruption. The co-VID velocity field maps for the first arrivals following the Hunga-Tonga eruption are shown in Fig. 2b–d, and the localization results are presented in Fig. 2e–f. Figure 2b shows the first velocity vectors at 04:23:30UT, i.e., 525s after the eruption onset time, both on the north-east and south-west out from the volcano. From the time of the first co-VID detection, in the NRT scenario, we need 22 minutes more to compute the first velocity field, which is an increase of the time delay for the NRT method as compared to 1-sec data. The two main reasons are a long 30-sec cross-correlation window (24 minutes vs. 5 minutes with 1-sec data) and sparse spatial resolution. The latter signifies fewer IPP that can be selected for correlation triangles after the first co-VID detection. Therefore, more time is necessary to "form" an interferometric triangle. The first vectors propagate in directions outward from the source. The first horizontal velocities of the co-VID are about ~830-900 m/s, i.e., they correspond to acoustic and shock-acoustic waves, and are in line with retrospective studies (e.g., Themens et al., 2022). The first velocity vectors are used to compute the first source location at the point with coordinates (17.90S; 176.26E) (Fig. 2e). The subsequent co-VID evolution during the next 2 minutes maintains the tendency for both the outward direction of propagation and velocities' values. Further, the velocities decrease to ~500-600 m/s, while the source locations concentrate northwest of the volcano (Fig. 2f).

3.1.2 Spatio-temporal characteristics of the co-VID from NRT TTD using 30-sec data.

The 30-sec NRT-TTD for all satellites and receivers (e.g, all LOS) is shown in Figure 3a. From these data, our newly developed fitting method estimates the velocity to be 621.1 m/s. This value is in line with previous retrospective observations for the ionospheric response to the Hunga-Tonga eruption (Themens et al., 2022), as well as with our "D1-GNSS-RT" results. The error of the velocity estimations is less than 10% for both NRT and Quasi-NRT method (Figure 3b,c). The difference between NRT and Quasi-NRT estimations is 11,1%. We can observe the existence of the co-VID signatures before the fitted slope line on Figure 3a, but the amplitudes of the disturbances were not sufficient for the "picker" part of the automatic NRT TTD fitting technique.

3.1.3 Spatio-temporal characteristics of the co-VID from NRT TTD using 1-sec data.

As mentioned above, only 16 GNSS receivers in the near-field of the HTHH volcano provided 1-sec data, which is too few to use the 1-sec "D1-GNSS-RT" method. Fortunately, these limits do not apply to NRT TTD. Figure 4 shows the dTEC/dt-based TTD plotted for the near-field co-VID. We note that the high-rate response to the HTHH volcanic eruption is more complex than the 30-sec one. Figure 5b demonstrates the occurrence of four dTEC/dt disturbances that are,

most likely, related to four independent eruptive events that occurred between 04:00 and 05:30 UT. The separate events can be distinguished on TTD based on the characteristics of the ionospheric responses, such as signal shape, the apparent velocity of propagation, and the amplitude.

The NRT TTD shows one quasi-periodic and three N-shaped signatures (dotted ovals in Figure 4b). The first quasi-periodic response (in the green circle) has the lowest velocity with respect to the other disturbances (~0.5 km/s). For the second response, the slope gives the apparent velocity of ~1.33 km/s. It appears to consist of three N-shaped signals which have identical velocity slopes. Further, we distinguish the third event based on a new increase in the dTEC/dt from ~05:15 UT. For this component, the velocity slope is ~2 km/s. Finally, the fourth event has an apparent velocity of ~1.33 km/s, which distinguishes it from the third event, although it is close in time.

Figure 4a shows an example of dTEC/dt signatures for receiver "SAMO" – satellite GLONASS R21 (in blue-white-red colormap). We also implement a centered moving average filter (5-sec window) to this series (black curve), which allow to remove noise in data and to concentrate on useful signals. These results prove an assumption of two types of the signatures: first, quasi-periodic and then, N-shaped ones. Evenmore, we observed the first co-VID driven signatures a couple of minutes before the USGS-determined eruption onset time (04:15 UT). Generally, it takes ~7-10 minutes for disturbances to reach the ionospheric altitudes, therefore the eruption onset occurred between 04:00 and 04:10 UT.

From our NRT-TTD, it is possible to estimate the onset times for all observed co-VID (Figure 4c). To do so, we first compute the intersection of the velocity slope line with the 0-km distance from the source. Second, we estimate the time in the intersection point from the TTD. This time corresponds to the onset time in the ionosphere, which is the time when the eruption-driven acoustic wave reaches the ionosphere (i.e., the altitude of detection, H_{ion} = 320 km). Third, we compute the vertical propagation time for the acoustic wave from the volcano to the ionosphere by using the sound speed profile derived from the NRLMSISE-2 model (Emmert et al., 2020). With a weighted average velocity of the sound speed of 470 m/s (Figure S3b), the acoustic wave will take ~11.34 minutes (11 minutes 20 seconds) to reach 320 km of altitude. Finally, we extract this propagation time from the ionospheric onset times in order to obtain the ground onset times for all four events (Table S1). From our method it follows that the HTHH volcano began to erupt at 04:08:26 UT, which is in agreement with satellite observations that suggest the eruption onset between 04:00 and 04:10 UT (Gusman and Rodger, 2022). Our onset time is also very close to that estimated by Astafyeva et al. (2022) from raw unfiltered TEC data by retrospective analysis. However, it is several minutes earlier than seismically-determined onset time (USGS; Poli & Shapiro, 2022), and ~20 minutes earlier than the onset estimated by using a pressure station at Tonga (Wright et al, 2022). Our work demonstrates that our ionosphere-based NRT approach can be successfully used along with conventional methods.

The occurrence of multiple eruptive events, that is clearly seen in dTEC/dt data, is in line with previous reports. For instance, Wright et al. (2022) identified four independent events that

252 occurred between 04:00 and 05:30 UT: 04:26 UT, 04:36 UT, 05:10 UT, 05:51 UT. Astafyeva et
253 al, 2022 suggested the occurrence of five eruptive events between 04:00 and 05:30 UT, however
254 their onset times differ from our estimations, which can be due to difference in the approximations
255 used.
256
257 **3.2 Far-Field ionospheric disturbance due to the Tonga Eruption.**
258
259 Previously, we applied our approach to the analysis of ionospheric response in the near-
260 field of the HTHH volcano and earthquakes (Maletckii & Astafyeva, 2021a). The near-field
261 ionospheric disturbances are usually characterized by relatively high velocities (e.g., 800-1200
262 m/s) and high frequencies (e.g., 4-10 mHz). In this section, we demonstrate how this approach and
263 our methods can perform in the Far-Field (i.e., several thousands of km away from the source) and
264 process traveling disturbances with lower velocities and frequencies. Perturbations with such
265 characteristics include tsunami-induced gravity waves. Therefore, the NRT-method can be used
266 for early warning systems.
267 To perform in the Far-Field, the following adjustments in our NRT fitting technique were
268 made: 1) the first maximum threshold is increased from 0.15 TECu/sec to 0.28 TECu/sec (for 30-
269 second data); 2) the velocity between two points should be in the range between 0.18 and 5 km/s.
270 The main reason to do so is to prevent "false detections". Since the ionosphere is an extremely
271 disturbed medium, different disturbances are always present at any place at any time moment. By
272 increasing the thresholds, we exclude disturbance not related to the eruption.
273 We apply the adjusted method to the detection of HTHH-driven disturbances in Japan,
274 North America and Chile, i.e. between 8,000 and 11,000 km away from the HTHH volcano (Figure
275 5).
276 We use the GEONET GNSS network to detect and characterize traveling ionospheric
277 disturbances on the Japanese coast (Animation S1). The 30-sec NRT-TTD for satellite GPS G07
278 and all available receivers is shown in Figure 5 (a-c). The first vivid signatures appeared at ~10:00
279 UT, ~6 hours after the first eruption. From these data, our newly developed fitting method
280 estimates the velocity to be 336.5 m/s, which is close to the Lamb wave speed, and is in line with
281 previous retrospective observations for the ionospheric response to the Hunga-Tonga eruption in
282 Japan (Themens et al., 2022; Zhang et. al., 2022).
283 The Lamb-wave driven ionospheric disturbances arrived on the West coast of North
284 America at ~12:00 UT, ~8 hours after the eruption onset (Animation S2). Figure 5 (d-f) shows 30-
285 sec NRT-TTD for satellite GPS G10 and all available receivers. Based on the TTD, our newly
286 developed fitting method estimates the velocity to be 365.9 m/s, which is slightly higher than the
287 Lamb wave, and is in agreement with retrospective analysis of the ionospheric response in North
288 America (Zhang et. al., 2022).
289 To study the response in the South-West Coast of South America (Animation S3), we used
290 1-sec data from the Centro Sismológico Nacional Universidad de Chile GNSS archives. The 1-sec
291 NRT-TTD for satellite GPS G18 is shown in Figure 5 (g-i). We also increased the threshold for

the picker up to 0.75 TECu/sec, since 1-sec data series are noisier and have larger peak-to-peak amplitudes than 30-sec data (Figure S1). The first disturbances arrive at ~12:00 UT, ~8 hours after the first eruption. From these data, our newly developed fitting method estimates the velocity to be 277.6 m/s. We attribute this disturbance to ionospheric response to the Lamb wave propagation.

3.3. Ionospheric disturbances driven by other events: small earthquake and explosion

To analyze the applicability and accuracy of the NRT-TTD method and the fitting technique, we analyze two events: 1) the M6.6 16 July 2007 Chuetsu earthquake in Japan, which is the smallest earthquake ever recorded in the ionosphere; 2) the 4 August 2020 Beirut explosion. Both events caused very weak TEC response as compared to the Tonga event (Figure S2).

The response to the Chūetsu earthquake as captured by satellite GPS G26 is presented in Figure 6 **(a)-(c).** Co-seismic ionospheric disturbances are seen ~10 minutes after the earthquake onset. We estimated their propagation speed to be 949.4 m/s, which is in agreement with the retrospective results (1 km/s by Cahyadi and Heki, 2015). The response to the Beirut explosion was captured by satellite GPS G22 (Figure 6 **(d)-(f))**. Clear N-shaped disturbances emerged ~12 minutes after the explosion onset and their velocity is estimated to be 883 m/s. Our estimation is in agreement with the retrospective estimations (0.8 km/s by Kundu et. al., 2021). We note that the spatial resolution of the GNSS network was very poor, which made it challenging to automatically process it, but our method succeeded.

4 Conclusions

In this work, we performed for the first time a near-real-time analysis of the ionospheric response to the massive 15 January 2022 Hunga Tonga-Hunga Ha'apai explosive eruption. Our main developments and findings are summarized below:

1. For the first time, we introduce a new method to determine spatio-temporal characteristics in the NRT. This method estimates the instantaneous velocities and the ionospheric source location using not only high-rate data but also the "conventional" 30-sec data. In addition, our new method can perform in sparse spatial coverage conditions. We note, however, that 30-sec data increase the NRT time delay between the event onset and the first results to ~30 minutes. By using this method, in a near-real-time scenario applied for the HTHH eruption case, we estimate the first instantaneous velocities to be ~800-900 m/s, which is in line with retrospective studies (e.g., Themens et al., 2022; Zhang et al., 2022), and correspond to acoustic and shock-acoustic waves. The location of the ionospheric source determined by our method is in the northwest of the volcano.
2. For the first time, we present a new method that can estimate the co-VID velocity from a real-time travel-time diagram. For the HTHH volcanic eruption, we observe the apparent co-VID propagation speed to be 621.1 m/s. This value is in line with our "D1-GNSS-RT" results. To further demonstrate the wide applicability of our method, we tested them on lower-amplitude

TEC responses in Japan, North America and Chile on the day of the HTHH eruption, and to the Beirut explosion of 4 August 2020, which was registered by a very sparse GNSS network, and the M6.6 Chuetsu earthquake of July 2007, which is the smallest earthquake ever registered in the ionosphere. In all cases, our method managed to capture the response and to correctly estimate the velocities.

3. Our dTEC/dt near-field NRT-TTD suggest the occurrence of four distinct eruptions between 04:00 and 05:30 UT. From the velocity slopes in NRT-TTD, we estimate the onset time for the four events at 04:08:43 UT, 04:31:00 UT, 05:02:30 UT, and 05:05:21 UT. The multi-eruption scenario is an agreement with the analysis of surface pressure data (Wright et al., 2022) and that of the unfiltered ionospheric TEC data (Astafyeva et al., 2022).
4. We emphasize that the amplitude of the dTEC/dt ionospheric response to the HTHH volcanic eruption is unprecedentedly strong: the peak-to-peak dTEC/dt disturbance amplitude exceeded by a factor of 2.5-3 all previously recorded co-VID. Such extreme values emphasize the unprecedented power of the HTHH volcano explosion, and are comparable to the ionospheric response to the 2011 Great Tohoku-Oki earthquake and the 28 October 2003 solar flare.

Our results once again demonstrate the advantages of the use of the dTEC/dt parameter as the effective NRT tool to rapidly determine dynamic characteristics of ionospheric disturbances. We also demonstrate that an ionosphere-based method can be a reliable alternative for detection of natural hazard events. This is especially important and useful for the analysis of submarine events, such as the HTHH volcanic eruption, where ground-based instrumentation is very limited.

Acknowledgments

We thank the French Space Agency (CNES, Project “RealDetect”) for the support. BM additionally thanks the CNES and the IPGP for the Ph.D. fellowship. We acknowledge the use of “tec-suite” codes developed by I. Zhivetiev (https://tec-suite.readthedocs.io/en/latest/).

We thank L. Rolland, P. Coïsson, D. Mikesell, M. Ravanelli, E. Munaibari & F. Manta for fruitful discussions within an ad-hoc Geoazur-IPGP-NGI working group on the 2022 Hunga Tonga volcano eruption.

Open Research

The Near-field and the Beirut explosion GNSS data are available from the CDDIS data archives (https://cddis.nasa.gov/archive/gnss/data/daily/). The Japan and the Chūetsu earthquake GNSS data are available from the GeoSpatial Authority of Japan (GSI, terras.go.jp). http://datahouse1.gsi.go.jp/terras/terras_english.html. The North America West Coast data are available from the UNAVCO data archives (https://data.unavco.org/archive/gnss/rinex/). The South America West Coast data are available from the Centro Sismológico Nacional Universidad de Chile data archives (http://gps.csn.uchile.cl/data/) and Instituto Geografico Nacional Argentino (https://www.ign.gob.ar/NuestrasActividades/Geodesia/Ramsac/DescargaRinex; Piñón et al., 2018)

Ionosonde station NIUE data are available from the DIDBase Web Portal (https://lgdc.uml.edu/common/DIDBMonthListForYearAndStation?ursiCode=ND61R&year=2022).

Figures were plotted by using Python (ver. 3.7, libraries "matplotlib.pyplot": https://matplotlib.org/3.5.0/api/_as_gen/matplotlib.pyplot.html and "cartopy": https://scitools.org.uk/cartopy/docs/latest/)

References

1. Astafyeva, E. (2019) Ionospheric detection of natural hazards. Reviews of Geophysics 57(4), 1265-1288. doi.org: 10.1029/2019RG000668
2. Astafyeva, E., Maletckii, B., Mikesell, T. D., Munaibari, E., Ravanelli, M., Coisson, P., et al. (2022). The 15 January 2022 Hunga Tonga eruption history as inferred from ionospheric observations. Geophysical Research Letters, 49, e2022GL098827. doi.org: 10.1029/2022GL098827
3. Astafyeva, E., Shalimov, S., Olshanskaya, E., & Lognonné, P. (2013). Ionospheric response to earthquakes of different magnitudes: Larger quakes perturb the ionosphere stronger and longer. Geophysical Research Letters, 40(9), 1675–1681. https://doi.org/10.1002/grl.50398
4. Calais, E. & Minster, J. B. (1995) GPS detection of ionospheric perturbations following the January 17, 1994, Northridge earthquake. Geophysical Research Letters, 22, 1045–1048. doi.org: 10.1029/95GL00168
5. Cahyadi, M. N. & Heki, K. (2015) Coseismic ionospheric disturbance of the large strike-slip earthquakes in North Sumatra in 2012: M_w dependence of the disturbance amplitudes, *Geophysical Journal International*, V. 200, I. 1, doi.org: 10.1093/gji/ggu343
6. Dautermann, T., Calais, E., & Mattioli, G. S. (2009). Global Positioning System detection and energy estimation of the ionospheric wave caused by the 13 July 2003 explosion of the Soufrière Hills Volcano, Montserrat. Journal of Geophysical Research, 114(B2), B02202. doi.org: 10.1029/2008JB005722
7. Emmert, J. T., Drob, D. P., Picone, J. M., Siskind, D. E., Jones, M., Mlynczak, M. G., et al. (2020). NRLMSISE 2.0: A whole-atmosphere empirical model of temperature and neutral species densities. *Earth and Space Science*, 8, e2020EA001321. doi.org: 10.1029/2020EA001321
8. Gusman, A.R. & Roger, J. (2022). Hunga Tonga - Hunga Ha'apai volcano-induced sea level oscillations and tsunami simulations. GNS Science webpage, doi.org: 10.21420/DYKJ-RK41
9. Heki, K. (2006) Explosion energy of the 2004 eruption of the Asama Volcano, central Japan, inferred from ionospheric disturbances, Geophys. Res. Lett., 33, L14303, doi: 10.1029/2006GL026249.
10. Kundu, B., Senapati, B., Matsushita, A. et al. (2021) Atmospheric wave energy of the 2020 August 4 explosion in Beirut, Lebanon, from ionospheric disturbances. Sci Rep 11, 2793. doi.org: 10.1038/s41598-021-82355-5
11. Liu, X., Zhang, Q., Shah, M., & Hong, Z. (2017). Atmospheric- ionospheric disturbances following the April 2015 Calbuco volcano from GPS and OMI observations. Advances in Space Research, 60 (12), 2836–2846. doi.org: 10.1016/j.asr.2017.07.007

12. Maletckii, B., Yasyukevich, Y., & Vesnin, A. (2020). Wave Signatures in Total Electron Content Variations: Filtering Problems. Remote Sensing, 12(8), 1340. doi.org: 10.3390/rs12081340
13. Maletckii, B. and Astafyeva, E. (2021a) Determining spatio-temporal characteristics of Coseismic Travelling Ionospheric Disturbances (CTID) in near real-time. Scientific Reports, 11:20783, doi: 10.1038/s41598-021-99906-5.
14. Maletckii, B. and Astafyeva, E. (2021b) Near-Real-Time Analysis of Spatio-Temporal Characteristics of Ionospheric Disturbances of Different Origins. *Session SA022, AGU Fall Meeting 2021, 13-17 December 2021, Hybrid, New Orleans, USA*
15. Manta, F., G. Occhipinti, E. Hill, A. Perttu, B. Taisne (2021) Correlation Between GNSS-TEC and Eruption Magnitude Supports the Use of Ionospheric Sensing to Complement Volcanic Hazard Assessment, J. Geophys. Res. - Solid Earth, doi: 10.1029/2020JB020726
16. R. Matoza, D. Lee, J.D. Assink, A.M. Iezzi, D.N. Green, et al. (**2022**) Atmospheric waves and global seismoacoustic observations of the January 2022 Hunga eruption, Tonga. *Science*, doi:10.1126/science.abo7063
17. Miyaki, K., Hayakawa, M. & Molchanov, O. A. (2002) The role of gravity waves in the lithosphere - ionosphere coupling, as revealed from the subionospheric LF propagation data. In Seismo Electromagnetics: Lithosphere - Atmosphere - Ionosphere Coupling; TERRAPUB: Tokyo
18. Nakashima, Y., Heki, K., Takeo, A., Cahyadi, M. N., Aditiya, A., & Yoshizawa, K. (2016). Atmospheric resonant oscillations by the 2014 eruption of the Kelud volcano, Indonesia, observed with the ionospheric total electron contents and seismic signals. Earth and Planetary Science Letters, 434, 112–116. doi.org: 10.1016/j.epsl.2015.11.029
19. Noll, C. E. & System, T. C. D. D. I. (2010) A resource to support scientific analysis using space geodesy. Adv. Space Res. 45(12), 1421–1440. doi.org: 10.1016/j.asr.2010.01.018 .
20. Poli, P., & Shapiro, N. M. (2022). Rapid characterization of large volcanic eruptions: Measuring the impulse of the Hunga Tonga Ha'apai explosion from teleseismic waves. Geophysical Research Letters, 49, e2022GL098123. doi.org: 10.1029/2022GL098123
21. RTCM. (2020) Radio Technical Commission for Maritime Services. https://www.rtcm.org/
22. Shults, K., E. Astafyeva and S. Adourian (2016). Ionospheric detection and localization of volcano eruptions on the example of the April 2015 Calbuco events. J. Geophys. Res. - Space Physics, V.121, N10, 10,303-10,315, doi.org: 10.1002/2016JA023382.
23. Themens, D. R., Watson, C., Žagar, N., Vasylkevych, S., Elvidge, S., McCaffrey, A., et al. (2022). Global propagation of ionospheric disturbances associated with the 2022 Tonga Volcanic Eruption. Geophysical Research Letters, 49, e2022GL098158. doi.org: 10.1029/2022GL098158
24. Takasu, T. (2013) RTKLIB: An Open Source Program Package for GNSS Positioning. http://www.rtklib.com
25. Wright, C.J., Hindley, N.P., Alexander, M.J. et al. (2022) Surface-to-space atmospheric waves from Hunga Tonga-Hunga Ha'apai eruption. Nature. doi.org: 10.1038/s41586-022-05012-5
26. Zhang, S.-R., et al. (2022) 2022 Tonga Volcanic Eruption Induced Global Propagation of Ionospheric Disturbances via Lamb Waves. Frontiers in Astronomy and Space Sciences, 8, doi.org: 10.3389/fspas.2022.871275

Figures Captions

Figure 1. Scheme of methods developed and implemented in this work. "D1-GNSS-RT" and NRT TTD methods require Real-Time TEC (can be transferred by RTKlib software (Takasu, 2013) and RTCM protocol (RTCM, 2020)) and orbits (can be obtained by Ultra-Rapid Orbits provided by IGS (Noll, 2010)) data. "D1-GNSS-RT" method calculates the instantaneous velocities' field and the direction of propagation for the detected disturbances. Based on these results, we compute the source location. NRT TTD estimates TID velocity and verifies the link with the source location. Panel **(b)** shows the difference in parameters between the 1-sec "D1-GNSS-RT" method that was developed previously Maletckii and Astafyeva (2021a) and 30-sec "D1-GNSS-RT" that was developed and implemented here for the first time.

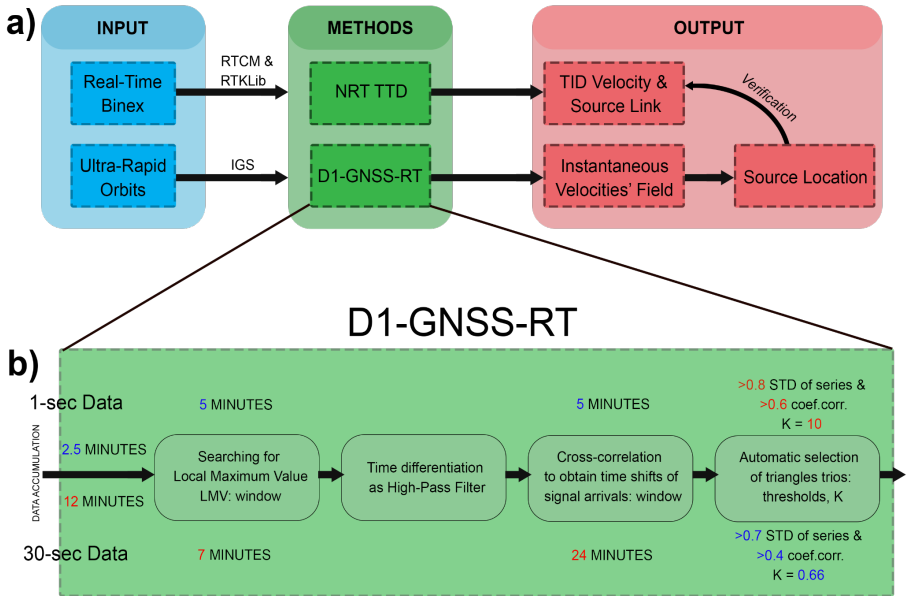

Figure 2. Geometry of near-field GNSS observations **(a)** and the results of the D1-GNSS-RT method **(b-f).** **(a)** The Hunga Tonga-Hunga Ha'apai volcano (red star, 175.382W; 20.53S) and GNSS receivers (yellow dots) network used in this work. The receivers that provide both 30 sec and 1 sec data are: "CKIS", "FAA1", "FTNA", "LAUT", "PTVL", "SAMO", "SOLO", "THTG", "TONG", "TOW2", "TUVA", "USP1". The others provide only 30 second data; **(b-d)** The first instantaneous velocities' field obtained by the "D1-GNSS-RT". Gray arrow denotes the velocity vector of 1000 m/s. The blue arrows correspond to the instantaneous velocities' field of co-VID; **(e-f)** the source locations (blue crosses) obtained from the instantaneous velocity vectors.

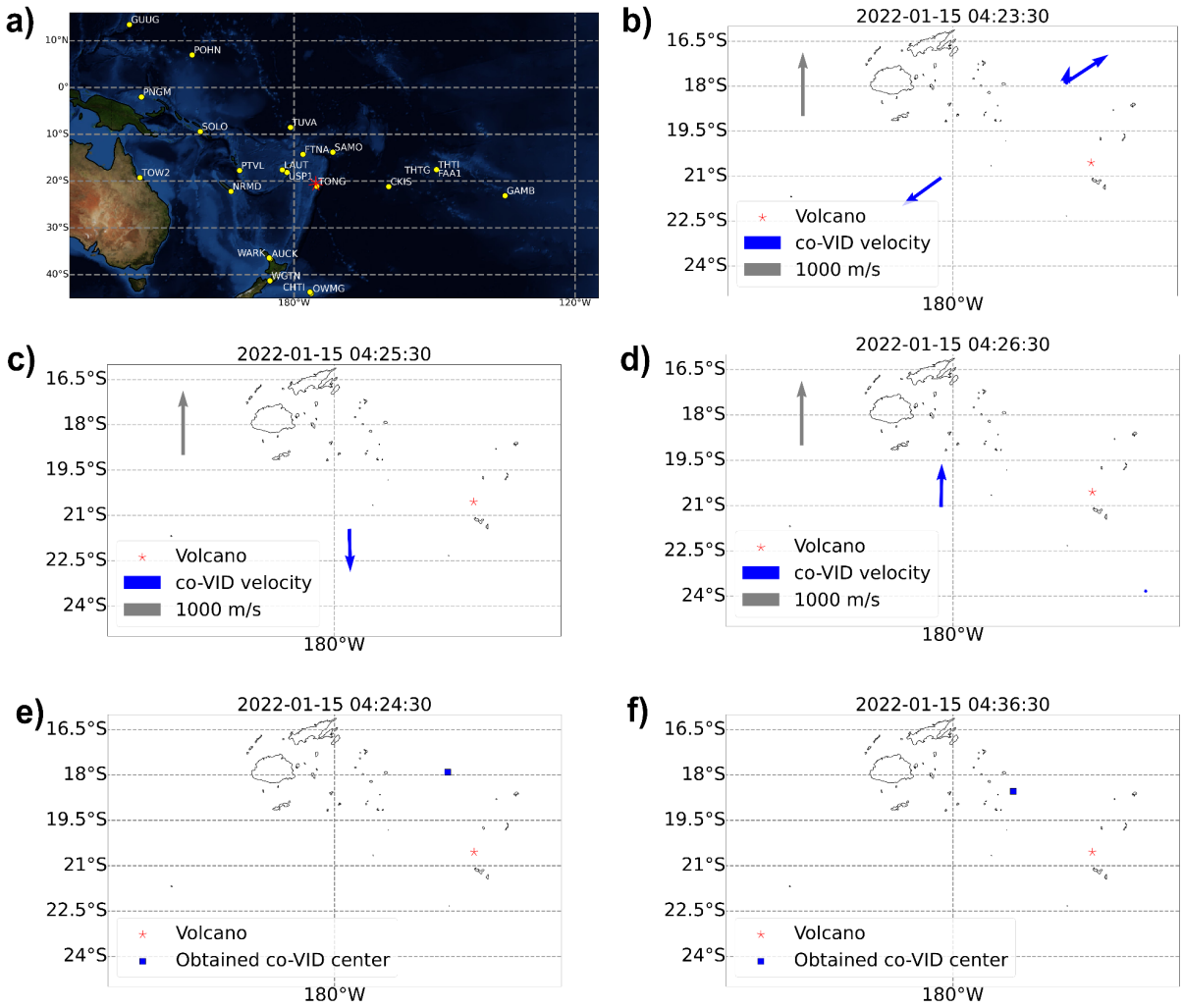

Figure 3. Application of NRT-TTD method to the near-field observations. **(a)** NRT TTD using 30-sec data and the estimated co-VID velocity (black line). Gray vertical line shows the USGS onset time at 04:15UT. The source is located in the Hunga Tonga-Hunga Ha'apai volcano. The black line was fitted by the newly developed automatic NRT-algorithm. **(b-c)** The two fitting algorithms that estimate the velocity from the TTD slope: **(b)** the NRT - the brown line, **(c)** the Quasi-NRT - purple. The blue dots correspond to the first maximums picked in each data series. The red and the green dots are used for the linear regression by the NRT and the Quasi-NRT algorithms, respectively.

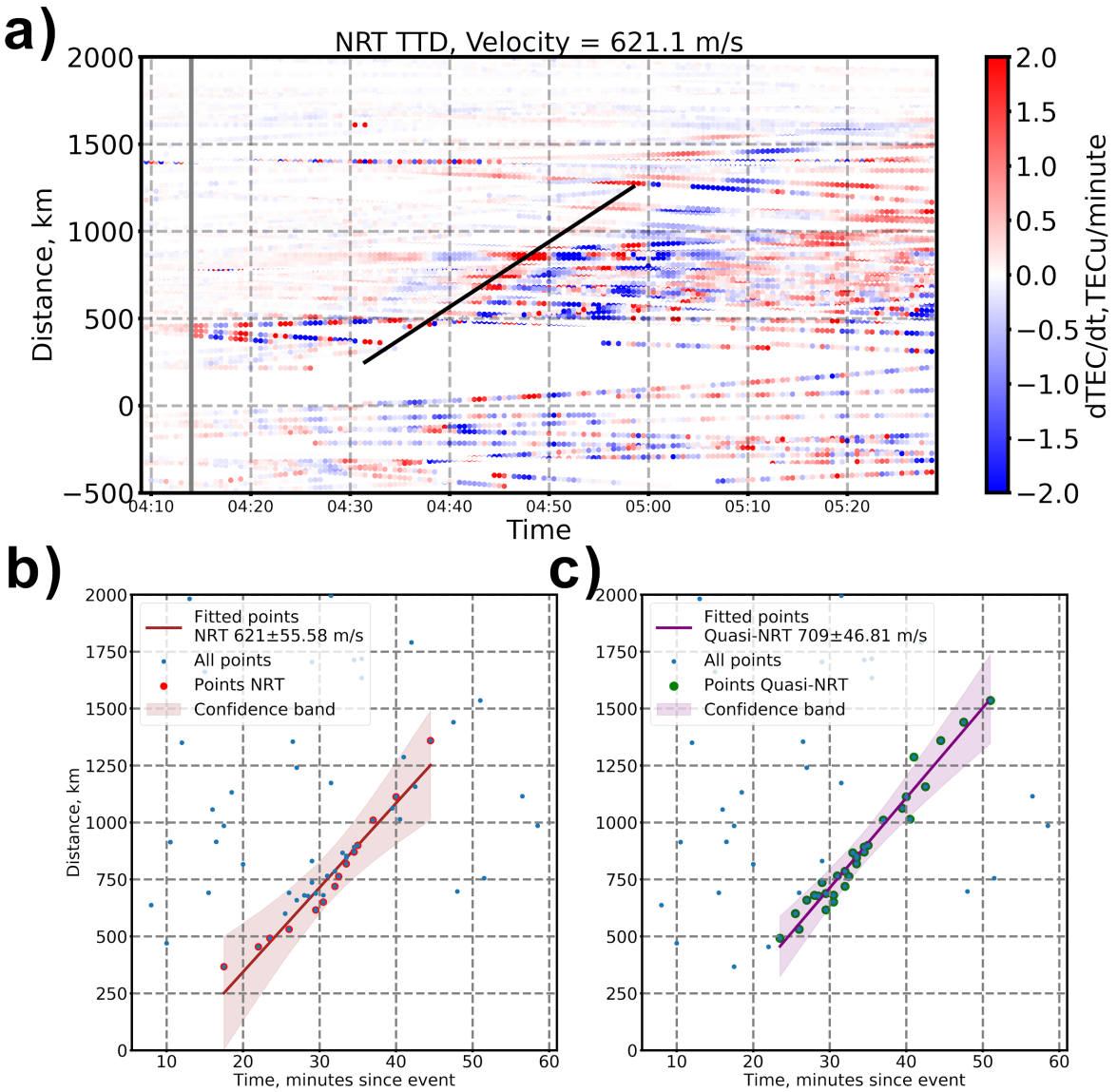

Figure 4. (**a**) dTEC/dt variations from a receiver "SAMO" - a satellite R21 LOS, blue-white-red curve - 1-sec data, black curve - 5 second centered smoothed data; **(b, c)** NRT TTD plotted using 1-sec data **(b)** and **(c)** zoom on the near-field dTEC/dt response from 04:00 to 05:30 UT. Gray

vertical line denotes the USGS onset time, the circles highlight four different disturbances detected in the near-field of the HTHH volcano (green - quasi-periodic signature, dark brown - N-shape ones). The slopes denote the apparent velocities of these four disturbances; **(d)** schematic representation of multi-eruption scenario and the onset time for each event

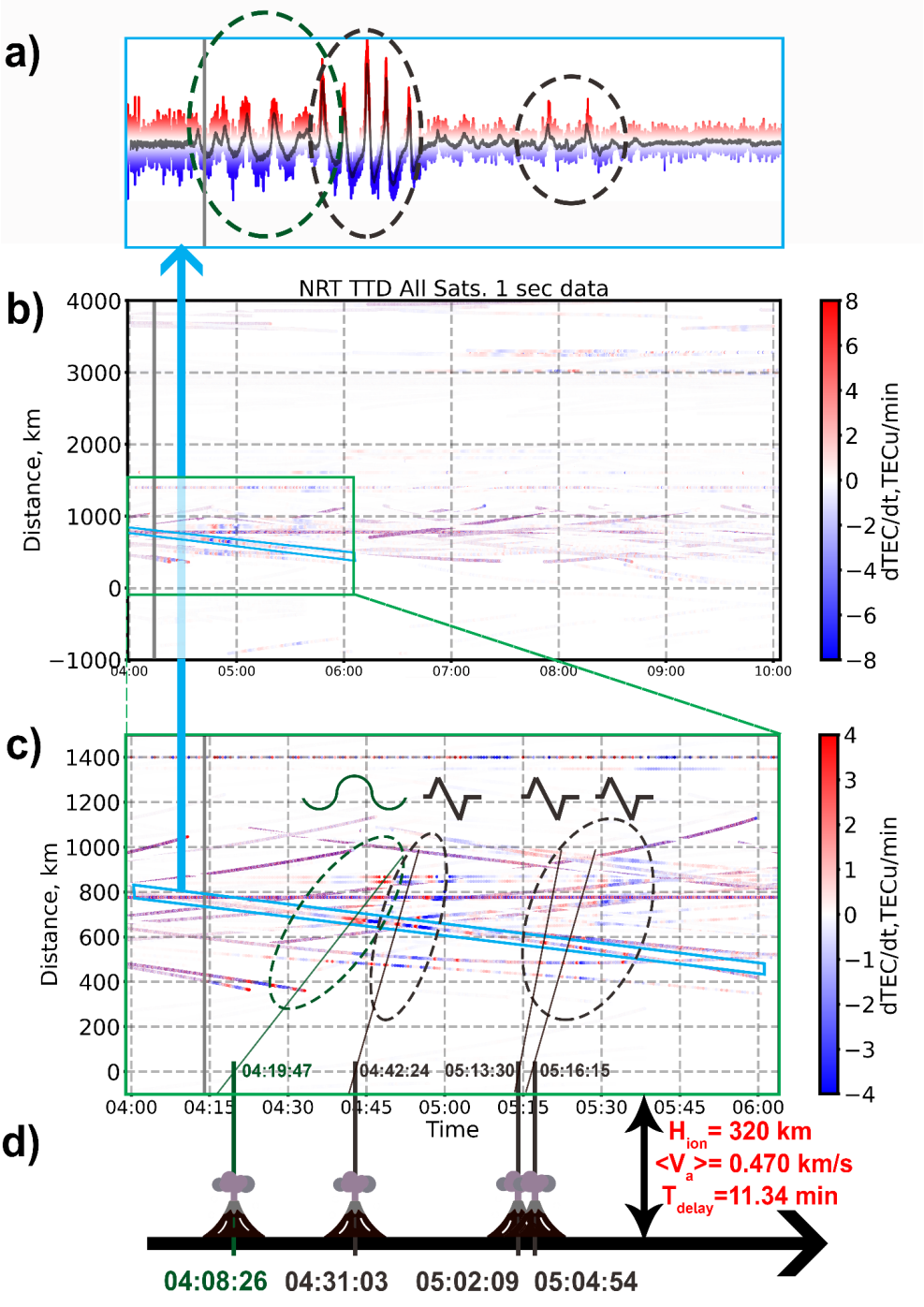

Figure 5. Application of NRT-TTD method to the far-field observations of ionospheric response. **(a,b,c)** the Japanese GNSS network and satellite GPS G07; **(d,e,f)** North American GNSS receivers and satellite GPS G10; **(g,h,i)** South American GNSS receivers and satellite GPS G10. The source is located in the Hunga Tonga-Hunga Ha'apai volcano. The black lines **(c,f,i)** were fitted by the automatic NRT-algorithm. The blue dots on panels **(a,b,d,e,g,h)** correspond to the first maxima of each series. The red and the green dots **(a,b,d,e,g,h)** are used for the linear regression by the NRT and the Quasi-NRT algorithms, respectively.

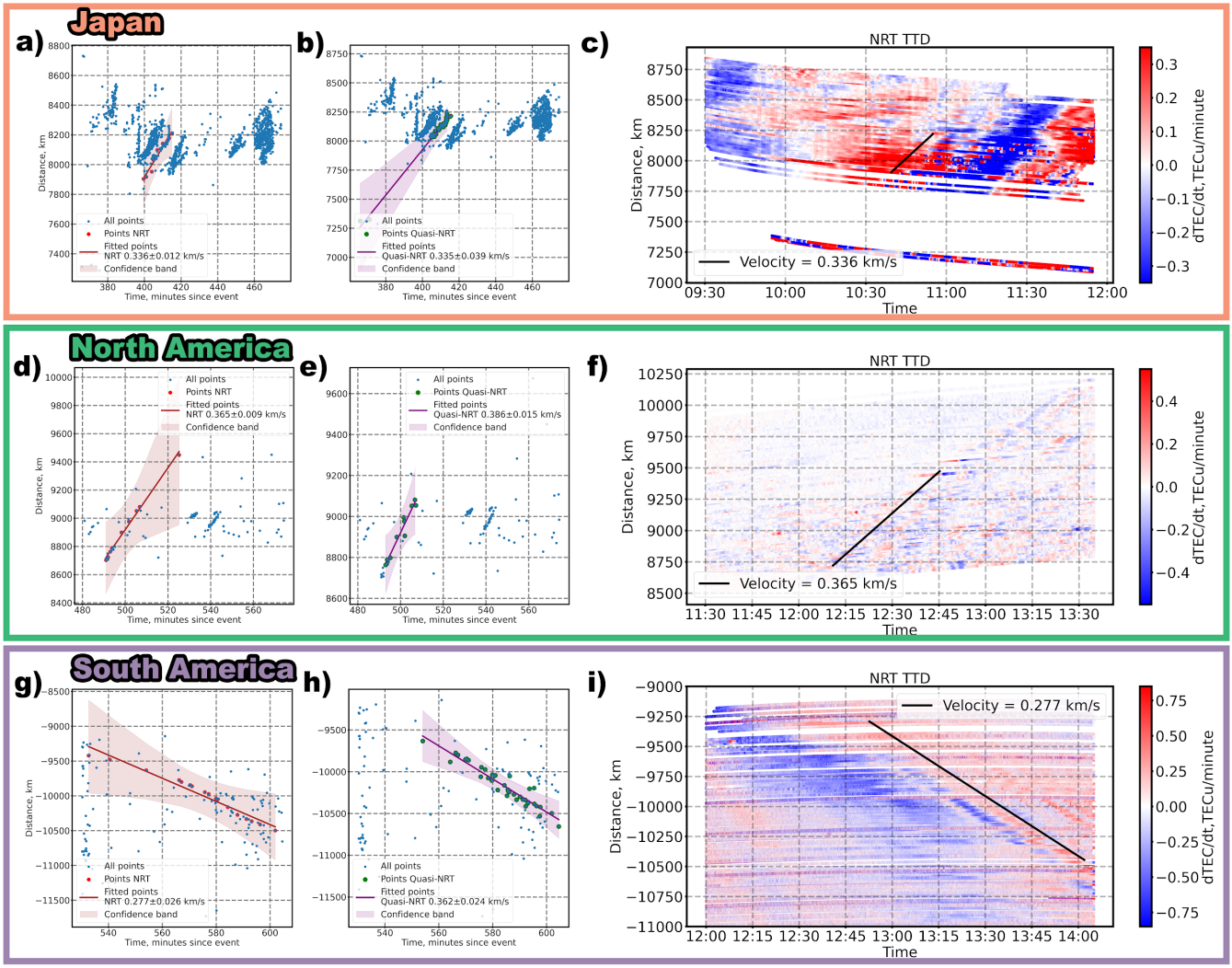

Figure 6. Application of NRT-TTD fitting technique to the M6.6 Chuetsu earthquake of 16 July 2007 **(a,b,c)** and the Beirut explosion of 4 August 2020 **(d,e,f).** The blue dots on panels **(b,c,e,f)** correspond to the first maxima of each series. The red **(b,e)** and the green **(c,f)** dots are used for the linear regression by the NRT and the Quasi-NRT algorithms, respectively. NRT velocity's

546 slope - the brown line on **(b,e)**, the black line on **(a,d)**; the Quasi-NRT **(c,f)** - purple, the event
547 onset time is indicated by a vertical gray line **(a,b)**.

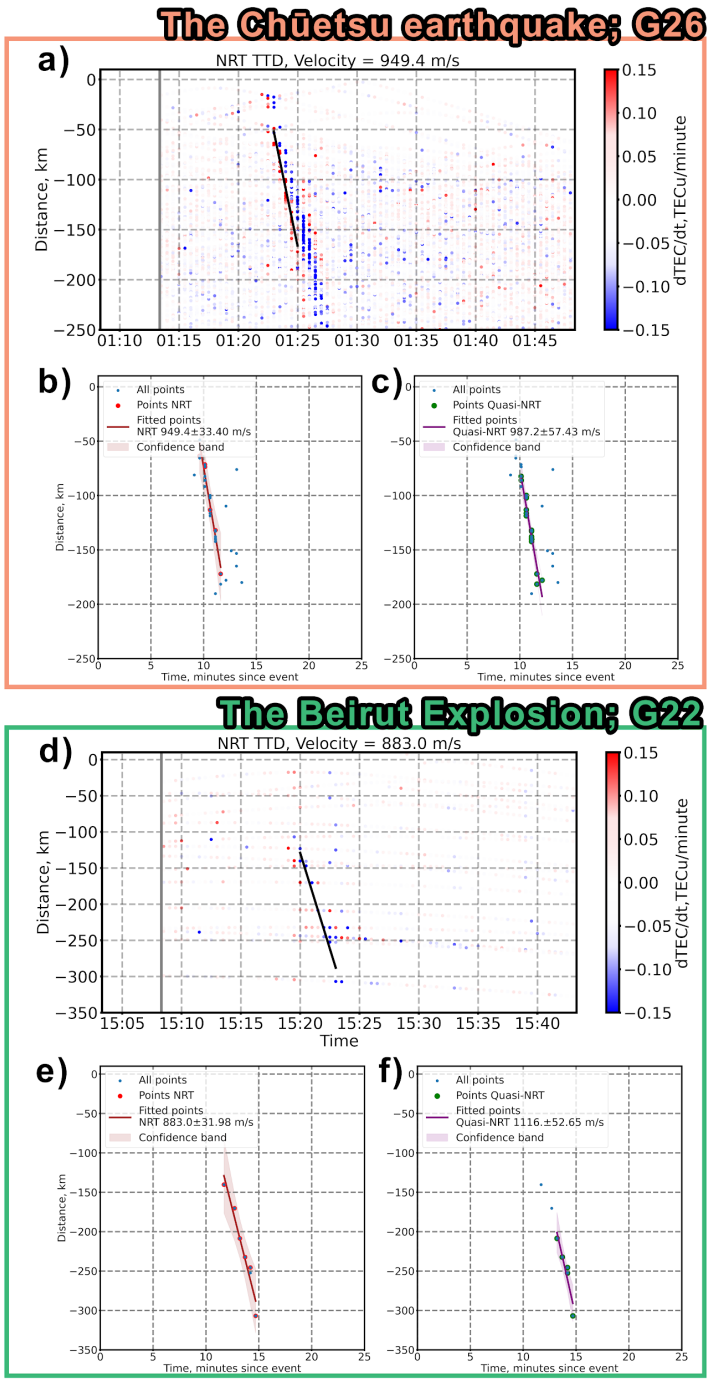

548